



2 Inversion solutions of the elliptic cone model for disk 3 frontside full halo coronal mass ejections

4 X. P. Zhao¹

5 Received 4 June 2007; revised 30 July 2007; accepted 10 October 2007; published XX Month 2008.

6 [1] A new algorithm is developed for inverting six unknown elliptic cone model
7 parameters from five observed CME halo parameters. It is shown that the halo parameter
8 α includes the information on the coronal mass ejection (CME) propagation direction
9 denoted by two model parameters. On the basis of the given halo parameter α , two
10 approaches are presented to find out the CME propagation direction. The two-point
11 approach uses two values of α observed simultaneously by COR1 and COR2 on board
12 STEREO A and B. The one-point approach combines the value of α with such
13 simultaneous observation as the location of CME-associated flare, which includes the
14 information associated with CME propagation direction. Model validation experiments
15 show that the CME propagation direction can be accurately determined using the two-
16 point approach, and the other four model parameters can also be well inverted,
17 especially when the projection angle is greater than 60° . The propagation direction and
18 other four model parameters obtained using the one-point approach for six disk frontside
19 full halo CMEs appear to be acceptable, though the final conclusion on its validation
20 should be made after STEREO data are available.

21 **Citation:** Zhao, X. P. (2008), Inversion solutions of the elliptic cone model for disk frontside full halo coronal mass ejections,
22 *J. Geophys. Res.*, 113, XXXXXX, doi:10.1029/2007JA012582.

24 1. Introduction

25 [2] Coronal mass ejections (CMEs) with an apparent
26 (sky-plane) angular width of 360° are called full halo
27 CMEs, and frontside full halo CMEs (FFH CMEs) if there
28 are near-surface activities associated with the full halo
29 CMEs. FFH CMEs with associated flares occurring within
30 45° and beyond 45° but within 90° from the solar disk
31 center are called, respectively, disk and limb FFH CMEs
32 [Gopalswamy *et al.*, 2003]. Disk FFH CMEs are mostly
33 symmetric and ellipse-like. Limb FFH CMEs are, however,
34 often asymmetric, including ragged structures as well as the
35 smooth structure. The ragged structures are believed to be
36 formed by the interaction between super-Alfvénic shocks
37 and preexisting coronal streamers and rays [Sheeley *et al.*,
38 2000]. This paper focuses on the inversion solution of the
39 elliptic cone model for disk FFH CMEs.

40 [3] Disk FFH CMEs have been shown to be the most
41 geoeffective kind of solar events. The geoeffectiveness rate
42 of total disk FFH CMEs between 1997 and 2005 reaches
43 75% [Gopalswamy *et al.*, 2007], supporting the earlier
44 result of 71% obtained using the disk FFH CMEs between
45 1997 and 2000 [Zhao and Webb, 2003]. It is the higher end
46 of the range of geoeffectiveness rate of solar activities. To
47 predict when and in what percentage a disk FFH CME
48 could generate intense geostorms, we need to determine

when and which part of the huge interplanetary counterpart 49
(ICME) of the disk FFH CME could hit Earth's magneto- 50
sphere. It requires the knowledge of the size, shape, 51
propagation direction and speed of ICMEs. However, coro- 52
nagraphs record only the total content of free electrons in 53
CMEs along the line of sight. A 2-D disk FFH CME cannot 54
unambiguously provide any real geometrical and kinematic 55
properties of a 3-D CME. 56

[4] CMEs are believed to be driven by free magnetic 57
energy stored in field-aligned electric currents, and before 58
eruption, the metastable structure with free magnetic energy 59
is confined by overlying arched field lines. The magnetic 60
configuration of most, if not all, CMEs is thus expected to 61
be magnetic flux ropes with two ends anchored on the solar 62
surface [e.g., Riley *et al.*, 2006], and the outer boundary of 63
the top (or leading) part of the ropes may be approximated 64
by an ellipse with its major axis aligned with the orientation 65
of the ropes. 66

[5] Most limb CMEs appear as planar looplike transients 67
with a radially pointed central axis and a constant angular 68
width. The existence of halo CMEs implies that the looplike 69
transients are three-dimensional. Both looplike and halolike 70
CMEs show the evidence of the rope-like magnetized 71
plasma structure of CMEs. A conical shell (or cone) model, 72
i.e., a hollow body which narrows to a point from a round, 73
flat base, was suggested to qualitatively understand the 74
formation of some full halo CMEs [Howard *et al.*, 1982]. 75

[6] The cone model, as a proxy of the rope-like magne- 76
tized plasma structure of CMEs, has been used to produce 77
modeled elliptic halos, and the model parameters that are 78
used to produce the modeled halos can be determined by 79

¹W. W. Hansen Experimental Physics Laboratory, Stanford University,
Stanford, California, USA.

80 matching modeled halos to observed halos [Zhao *et al.*,
81 2002]. The three model parameters of the circular cone
82 model can also be directly inverted from three halo param-
83 eters that characterize 2-D elliptic halos [Xie *et al.*, 2004].

84 [7] The geometrical and kinematical properties obtained
85 using the circular cone model for the 12 May 1997 disk
86 FFH CME [Zhao *et al.*, 2002] were introduced at the
87 boundary of a 3-D MHD solar wind model [Odstrcil and
88 Pizzo, 1999], and the associated ICME near the Earth's orbit
89 were successfully reproduced [Odstrcil *et al.*, 2004]. It
90 indicates that the idea for using cone-like geometric model
91 to invert model parameters from halo parameters is valid
92 and useful in estimating the real geometrical and kinemat-
93 ical properties for disk FFH CMEs.

94 [8] It was found that the circular cone model can be used
95 to reproduce only a limited cases of halo CMEs, and that the
96 elliptic cone model, i.e., a body which narrows to an apex
97 from an elliptic, flat base, would be better than the circular
98 cone model in approximating the rope-like CMEs [Zhao,
99 2005; Cremades and Bothmer, 2005]. However, the inver-
100 sion solution of the elliptic cone model obtained using the
101 approaches of both Zhao [2005] and Cremades and
102 Bothmer [2005] are often not unique.

103 [9] In what follows we first define five halo parameters
104 and three halo types for disk FFH CMEs in section 2. We
105 then develop a new elliptic cone model with six model
106 parameters, and produce modeled halos that are expected to
107 be observed by multi-spacecraft, such as STEREO A,
108 SOHO, and STEREO B in section 3. The inversion equation
109 system of the elliptic cone model and the expressions of its
110 solution are established in section 4. On the basis of two-
111 point and one-point observations of CMEs, two approaches
112 are presented in section 5 for determining the CME prop-
113 agation direction and other model parameters, and the
114 model validation experiment is carried out to see whether
115 or not the established inversion equation system and the two
116 approaches are acceptable and useful. Finally we summarize
117 and discuss the results in section 6.

118 2. Description and Classification of Observed 119 Elliptic Halos

120 [10] Figure 1 displays six disk FFH CMEs selected from
121 Table 3 of Cremades [2005]. The onset date of the six
122 events is shown on the top of each panel.

123 2.1. Five Halo Parameters: D_{se} , α , SA_{xh} , SA_{yh} , and ψ

124 [11] The white oval curve in each panel of Figure 1 is
125 obtained by fitting to five selected points along the outer
126 edge of each CME halo (see Cremades [2005] for details).
127 All white curves are ellipses and occur on the sky-plane
128 $Y_h Z_h$ where Y_h and Z_h are the axes of the heliocentric
129 ecliptic coordinate system, pointing to the west and north,
130 respectively.

131 [12] As shown in each panel, the short thick green line,
132 D_{se} , denotes the distance between the solar disk center and
133 the elliptic halo center, and axes X'_c and Y'_c are aligned with
134 and perpendicular to D_{se} , respectively. The location of
135 elliptic halos on the sky-plane can be specified using
136 parameter D_{se} and the angle α between axes X'_c and Y_h .
137 The shape and size of elliptic halos can be specified using
138 two semi-axes of the halos, SA_{xh} and SA_{yh} , where SA_{xh} and

SA_{yh} are located near the axes X'_c and Y'_c , respectively. The
139 orientation of elliptic halos can thus be specified by the
140 angle ψ between X'_c and SA_{xh} or Y'_c and SA_{yh} .

141 [13] The five halo parameters, SA_{xh} , SA_{yh} , D_{se} , α and ψ ,
142 can be measured once the outer edge of halo CMEs is
143 recognized. The top of each panel in Figure 1 shows the
144 measured values of the five halo parameters for each event.
145

146 2.2. Halo Equations

147 [14] By using four halo parameters SA_{xh} , SA_{yh} , D_{se} and ψ ,
148 a 2-D elliptic halo on the plane $X'_c Y'_c$ can be expressed

$$\begin{bmatrix} x'_c \\ y'_c \end{bmatrix} = \begin{bmatrix} D_{se} \\ 0 \end{bmatrix} + \begin{bmatrix} \cos \psi & \sin \psi \\ -\sin \psi & \cos \psi \end{bmatrix} \begin{bmatrix} x_{eh} \\ y_{eh} \end{bmatrix} \quad (1)$$

149 where

$$\begin{bmatrix} x_{eh} \\ y_{eh} \end{bmatrix} = \begin{bmatrix} SA_{xh} \sin \delta_h \\ SA_{yh} \cos \delta_h \end{bmatrix} \quad (2)$$

150 The symbol δ_h in equation (2) is the angle of radii of elliptic
151 halos relative to SA_{yh} axis, and increases clockwise along an
152 elliptic rim from 0° to 360° .

153 [15] The halo observed in the sky-plane $Y_h Z_h$ can be
154 obtained by rotating an angle of α as follows

$$\begin{bmatrix} y_h \\ z_h \end{bmatrix} = \begin{bmatrix} \cos \alpha & \sin \alpha \\ -\sin \alpha & \cos \alpha \end{bmatrix} \begin{bmatrix} x'_c \\ y'_c \end{bmatrix} \quad (3)$$

155 2.3. Three Types of Observed Halos

156 [16] It has been shown that the semi minor (major) axis of
157 the elliptic halos formed by the circular cone model must be
158 aligned with X'_c (Y'_c) axis. In other words, the halo param-
159 eter ψ must be equal to zero (see Xie *et al.* [2004] and Zhao
160 *et al.* [2002, Figure 2] for details). Because of the uncer-
161 tainty in identifying elliptic halos from coronagraph CME
162 images, we consider SA_{xh} being nearly aligned with X'_c if
163 $|\psi| < 10^\circ$.

164 [17] Figure 1 shows that the halo parameter ψ that
165 characterizes the orientation of elliptic halos can be any
166 value between -45° and 45° . It means that the semi major
167 (or minor) axis can be located anywhere on the plane of
168 $X'_c Y'_c$. This fact suggests that most of disk FFH CMEs
169 cannot be fitted or inverted using the circular cone model.

170 [18] To distinguish the halos that may be inverted using
171 the circular cone model from the halos that can be inverted
172 using the elliptic cone model, we classify the observed
173 elliptic halos into the following three types:

Type A : $|\psi| < 10^\circ, SA_{xh} < SA_{yh}$;

Type B : $|\psi| < 10^\circ, SA_{xh} \geq SA_{yh}$;

Type C : $10^\circ \leq |\psi| \leq 45^\circ$.

180 [19] The top left panel of Figure 1 shows a sample of
181 Type A halo where SA_{xh} denotes the semi minor axis and is

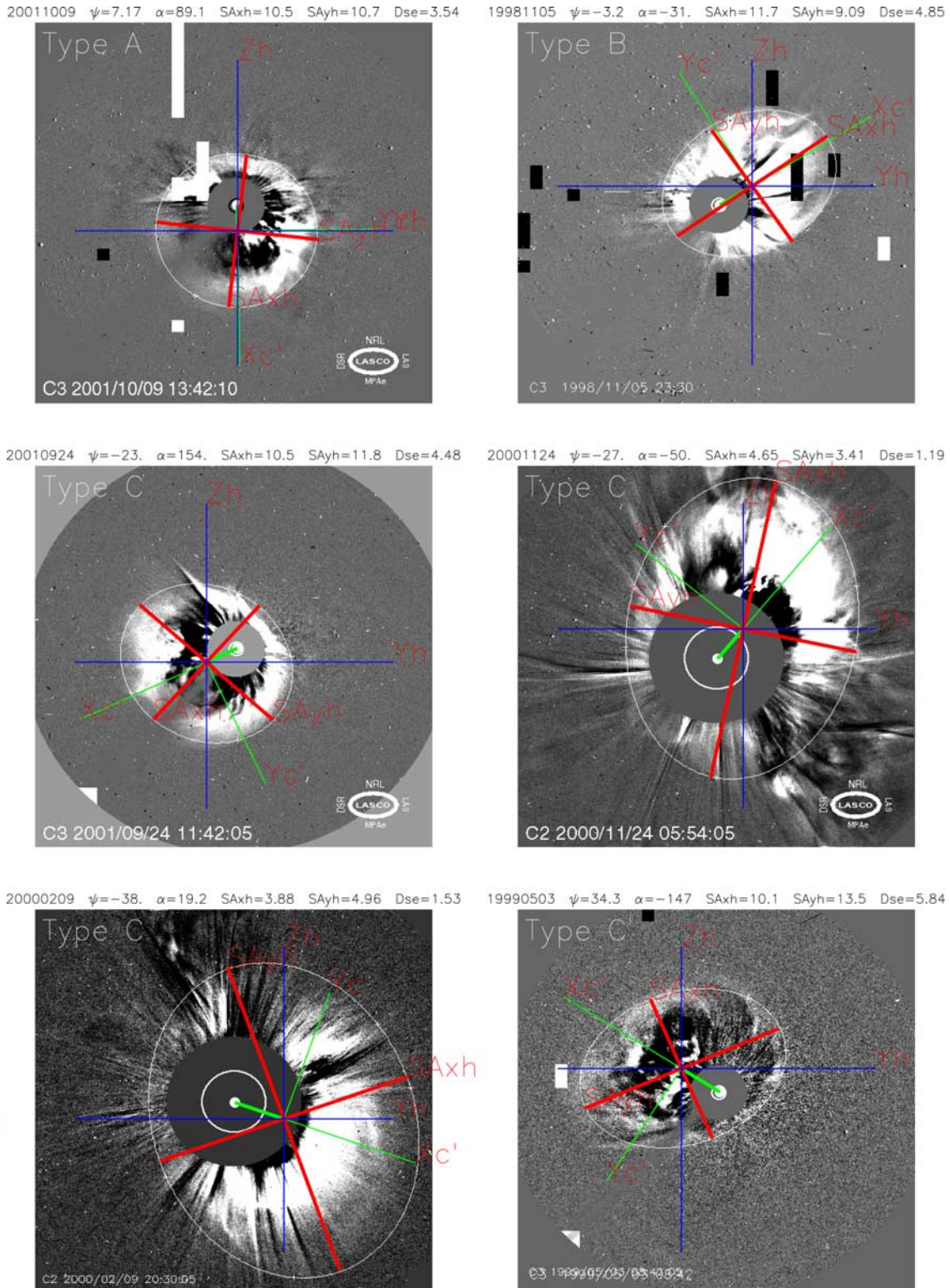


Figure 1. Definition of five halo parameters (SA_{xh} , SA_{yh} , ψ , D_{se} , and α) and Types A, B, and C for disk frontside full halo CMEs (see text for details). Here X'_c and Y'_c are, respectively, aligned with and perpendicular to the direction from the solar disk center to the halo center, D_{se} (the short thick green line). Parameters ψ and α denote the angles between SA_{yh} and Y'_c and between X'_c and Y_h , respectively.

182 nearly aligned with X'_c axis. The Type A halo may be
 183 formed by the circular or the elliptic cone model. The top
 184 right panel shows a sample of Type B halo where SA_{xh}
 185 denotes the semi major axis though it is nearly aligned with

X'_c . The four events shown in middle and bottom rows are
 186 Type C halos. Both Type B and Type C halos certainly
 187 cannot be produced using the circular cone model, and their
 188

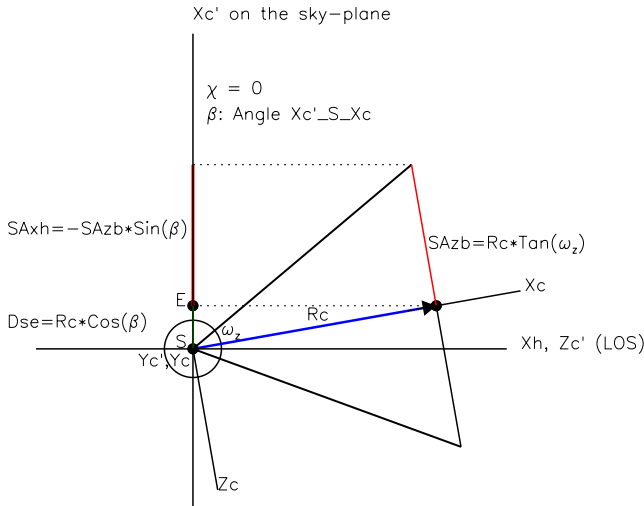


Figure 2. Three coordinate systems used in the transformation from the cone coordinate system $X_c Y_c Z_c$ through the projection coordinate system $X'_c Y'_c Z'_c$ to the heliocentric ecliptic coordinate system $X_h Y_h Z_h$. The projection of the elliptic cone base onto the sky-plane takes place from $X_c Y_c Z_c$ to $X'_c Y'_c Z'_c$ and depends only on the parameter β , the angle from X_c to X'_c . The circle with a radius of 2 denotes the occulting disk of Coronagraph C2 on board SOHO.

189 model parameters must be inverted using the elliptic cone
190 model.

191 [20] Among 30 events in Table 3 of *Cremades* [2005], the
192 number of Types A, B, and C is 3, 7 and 20, respectively.
193 This distribution implies that only 10% of disk FFH CMEs
194 may be reproduced and inverted using the circular cone
195 model. Since Type A halos may also be formed by the
196 elliptic cone model as shown in sections 4 and 5, the model
197 parameters inverted using the circular cone model for some
198 Type A halos may significantly differ from the real ones.

200 3. Elliptic Cone Model and Model Parameters

201 [21] Since the shape of 3-D rope-like CME plasma
202 structure may be better approximated using the elliptic cone
203 model, halos formed on the sky-plane by Thompson scatter-
204 ing along the line-of-sight may be better reproduced by
205 projecting the elliptic cone base onto the sky-plane.

206 3.1. Six Elliptic Cone Model Parameters: λ , ϕ , R_c , ω_y , 207 ω_z , and χ

208 [22] As mentioned in section 1, the elliptic cone model is
209 a hollow body which narrows to its apex from an elliptic,
210 flat base. The position of an elliptic cone base in the
211 heliocentric ecliptic coordinate system, $X_h Y_h Z_h$, can be
212 determined by locating the apex of the elliptic cone at the
213 origin of the $X_h Y_h Z_h$ system, and by specifying the direction
214 of the central axis of the elliptic cone in the $X_h Y_h Z_h$ with
215 latitude λ and longitude ϕ . Here the X_h axis is aligned with
216 the line-of-sight, pointing to the Earth; λ and ϕ are mea-
217 sured with respect to the ecliptic plane $X_h Y_h$ and the line-of-
218 sight X_h , respectively.

219 [23] To define the size, shape and orientation of elliptic
220 cone bases we introduce a ‘‘cone coordinate system,’’

$X_c Y_c Z_c$, and a ‘‘projection coordinate system,’’ $X'_c Y'_c Z'_c$ (see
Figure 2 for the definition of the three axes). As shown in
Figure 2 and the left column of Figures 3 and 4, the distance
between the base and apex is denoted by R_c , and the half
angular widths corresponding to two semi-axes of the cone
bases, SA_{yb} and SA_{zb} , are by ω_y and ω_z . As shown in the
bottom panel of the left column of Figures 3 and 4, the
angle, χ , between SA_{yb} and Y_c or between SA_{zb} and Z_c axes,
specifies the orientation of the cone base. Therefore six
model parameters are needed to characterize the location,
the shape and size, and the orientation of the base of a 3-D
elliptic cone model in the $X_h Y_h Z_h$ system.

233 3.2. Relationship Between λ , ϕ and β , α

[24] As shown in Figures 1 and 2, the projection angle β ,
i.e., the angle between the central axis X_c and its projection
on the sky-plane, X'_c , denotes the latitude of the central axis
relative to the sky-plane, and the observed halo parameter α
the longitude of the central axis relative to westward Y_h .

[25] The relationship between (β, α) and (λ, ϕ) is

$$\begin{cases} \sin \lambda = \cos \beta \sin \alpha \\ \tan \phi = \cos \alpha / \tan \beta \end{cases} \begin{cases} \sin \beta = \cos \lambda \cos \phi \\ \tan \alpha = \tan \lambda / \sin \phi \end{cases} \quad (4)$$

Equation (4) shows that parameter α (and β) depends on
both λ and ϕ . Therefore the observed halo parameter α
provides information of both λ and ϕ . This information will
be used in finding out the unknown parameter β , as shown
in section 5. It should be noted that positive angles are
measured counterclockwise in rotation transformation.

[26] In fact, the projection of the elliptic cone base onto
the sky-plane depends only on the projection angle, β . We
will replace λ and ϕ by β in establishing the inversion
equation system of the elliptic cone model.

251 3.3. Projection of the Elliptic Cone Base on the 252 Sky-Plane

[27] Given a set of values for the five model parameters
 R_c , ω_y , ω_z , χ , β , a modeled halo on the plane $X'_c Y'_c$
can be obtained by the transformation of the rim of the elliptic
cone base from coordinate system $X_c Y_c Z_c$ to $X'_c Y'_c Z'_c$ and
from $X_c Y_c Z_c$ to $X'_c Y'_c Z'_c$,

$$\begin{bmatrix} x'_c \\ y'_c \\ z'_c \end{bmatrix} = \begin{bmatrix} \cos \beta & -\sin \beta \sin \chi & -\sin \beta \cos \chi \\ 0 & -\cos \chi & -\sin \chi \\ \sin \beta & -\cos \beta \sin \chi & \cos \beta \cos \chi \end{bmatrix} \begin{bmatrix} x_{eb} \\ y_{eb} \\ z_{eb} \end{bmatrix} \quad (5)$$

$$\begin{bmatrix} x_{eb} \\ y_{eb} \\ z_{eb} \end{bmatrix} = \begin{bmatrix} R_c \\ R_c \tan \omega_y \cos \delta_b \\ R_c \tan \omega_z \sin \delta_b \end{bmatrix} \quad (6)$$

where the symbol δ_b is the angle of radii of an elliptic base
relative to SA_{yb} axis and increase along the rim of the elliptic
base from 0° to 360° .

[28] Using parameter α and equation (3), the modeled
halo on the plane $Y_h Z_h$ can be obtained.

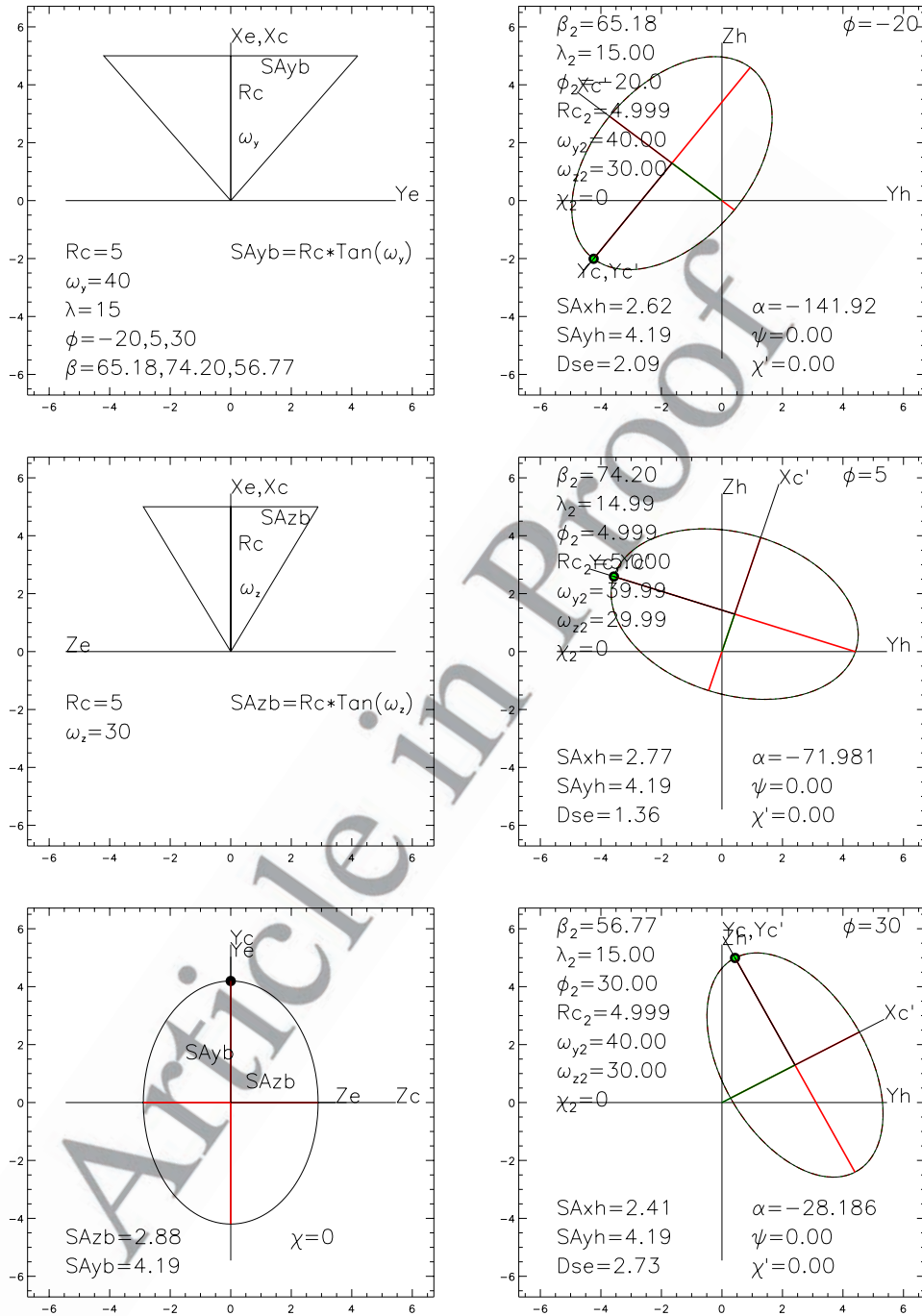


Figure 3. The left column shows the definition of elliptic cone model parameters R_c , ω_y , ω_z , and χ , and a set of values for six elliptic cone model parameters. The right column shows the three modeled halos (black ellipses) that are supposed to be observed by three spacecraft located on the ecliptic plane with different azimuths. The inverted model parameters with subscript "2" are also shown in each panel in the right column. The green and red dashed ellipses are modeled halos calculated using inverted elliptic and circular cone model parameters, respectively.

266 **3.4. Modeled Halos**

267 [29] Given a set of model parameters λ , ϕ , ω_y , ω_z , R_c and
 268 χ , as shown in the left column of Figures 3 and 4, we first
 269 calculate β and α using λ , ϕ and equation (4), then predict
 270 the elliptic halo on the sky-plane using equations (5), (6)
 271 and (3). The black ellipses in the right column of Figures 3
 272 and 4 show the modeled halos that are expected to be

observed by coronagraphs on board three spacecraft, say, 273
 STEREO A, SOHO, and STEREO B, simultaneously. As 274
 shown in each panel of the right column in Figures 3 and 4, 275
 the five halo parameters SA_{xh} , SA_{yh} , D_{se} , ψ , and α can be 276
 calculated on the basis of the modeled halos. 277

[30] The small green and big black dots in each panel 278
 denote, respectively, the semi axis of the modeled halos 279

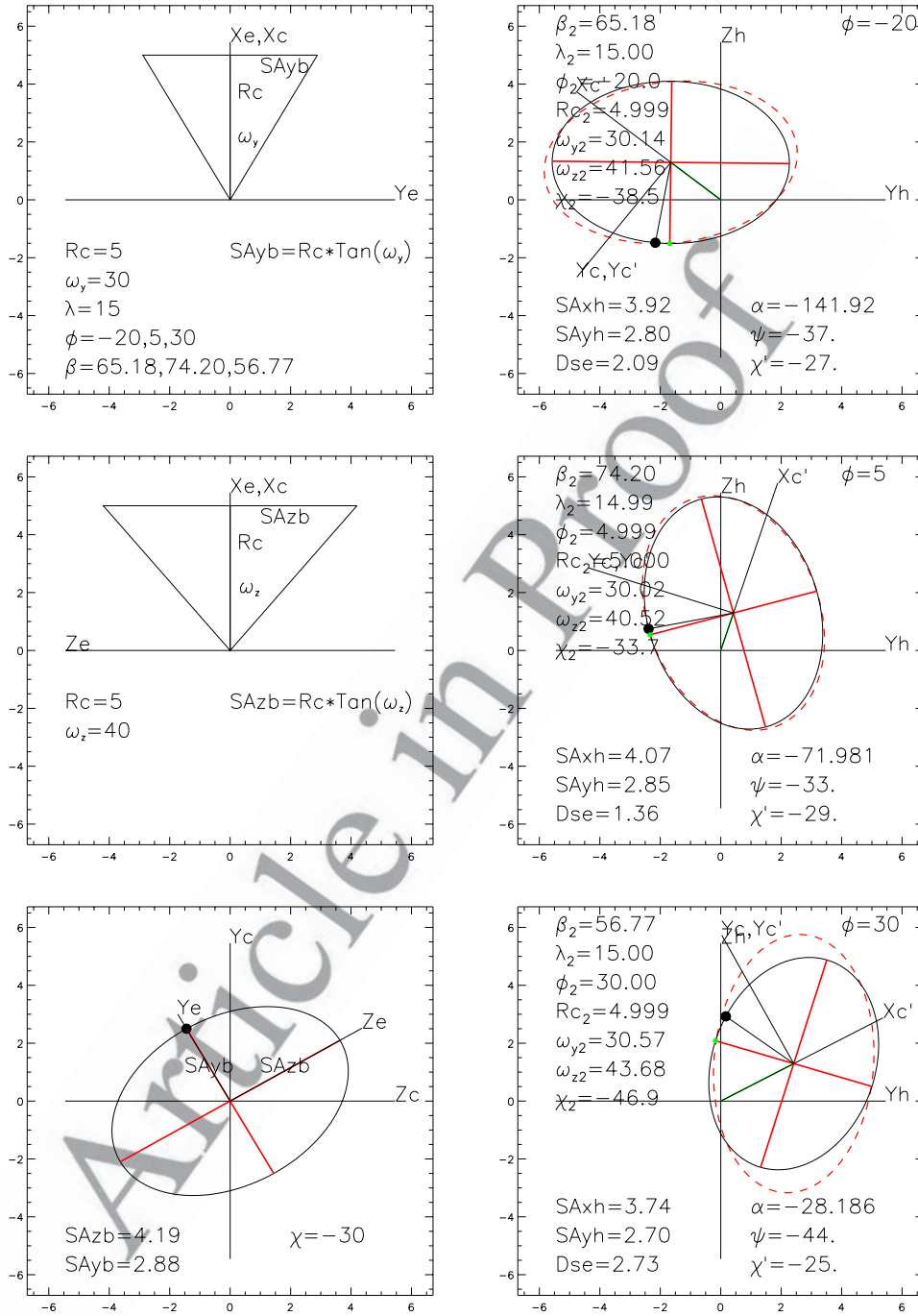


Figure 4. The same as Figure 3 but with different ω_y , ω_z , and χ , as shown in the left column.

280 located near the Y'_c axis and the projection of the base semi-
 281 axis SA_{yb} on the $Y_h Z_h$ plane. Parameters ψ and χ' denote,
 282 respectively, the angular distance of the green and black
 283 dots from the Y'_c axis. The values of ψ and χ' in Figures 3
 284 and 4 depend on χ and β . The difference $\chi' - \chi$ and $\psi - \chi$
 285 show the effect of the projection. Both χ' and ψ are zero
 286 when $\chi = 0$ (see Figure 3).

288 **4. Inversion Equation System and Its Solution**

289 [31] In order to invert the unknown model parameters
 290 from observed halo parameters, we first establish the

inversion equation system that relates model parameters
 with halo parameters. We then find out the solution of the
 inversion equation system.

294 **4.1. Inversion Equation System of the**
 295 **Elliptic Cone Model**

[32] The inversion equation system of the elliptic cone
 model may be established by comparing observed and
 modeled halos on the plane of $X'_c Y'_c$. Equations (1) and
 (2) describe observed elliptic halos on the plane of $X'_c Y'_c$
 using four halo parameters SA_{xh} , SA_{yh} , D_{se} , ψ . Equations (5)
 and (6) are the expressions of modeled elliptic halos on the

302 same plane, but using five model parameters R_c , ω_y , ω_z , χ ,
303 and β .

304 [33] By comparing the like items between equations (1)
305 and (5), and setting $\delta_h = \delta_b + \Delta\delta$, the relationship between
306 elliptic cone model parameters and elliptic CME halo
307 parameters can be established

$$\begin{aligned} R_c \cos \beta &= D_{se} \\ R_c \tan \omega_y \sin \beta \sin \chi &= SA_{xh} \cos \psi \sin \Delta\delta + SA_{yh} \sin \psi \cos \Delta\delta \\ -R_c \tan \omega_z \sin \beta \cos \chi &= SA_{xh} \cos \psi \cos \Delta\delta - SA_{yh} \sin \psi \sin \Delta\delta \\ R_c \tan \omega_y \cos \chi &= -SA_{xh} \sin \psi \sin \Delta\delta + SA_{yh} \cos \psi \cos \Delta\delta \end{aligned} \quad (7)$$

309 All model (halo) parameters occur in left (right) side of the
310 equation system (7). By assuming $\Delta\delta = \delta_h - \delta_b \simeq \psi - \chi$,
311 we have

$$\begin{aligned} R_c \cos \beta &= D_{se} \\ (R_c \tan \omega_y \sin \beta + a) \tan \chi &= b \\ -R_c \tan \omega_z \sin \beta - b \tan \chi &= a \\ R_c \tan \omega_y - b \tan \chi &= c \end{aligned} \quad (8)$$

313 where

$$\begin{aligned} a &= SA_{xh} \cos^2 \psi - SA_{yh} \sin^2 \psi \\ b &= (SA_{xh} + SA_{yh}) \sin \psi \cos \psi \\ c &= -SA_{xh} \sin^2 \psi + SA_{yh} \cos^2 \psi \end{aligned} \quad (9)$$

316 [34] For Types A and B FFH CMEs, $\psi = 0$ and $\chi = 0$,
317 equation systems (8), (9) become

$$\begin{aligned} R_c \cos \beta &= D_{se} \\ -R_c \tan \omega_z \sin \beta &= SA_{xh} \\ R_c \tan \omega_y &= SA_{yh} \end{aligned} \quad (10)$$

319 and when $\omega_y = \omega_z$, the number of model parameters equals
320 the number of halo parameters, equation system (10) reduce
321 to the inversion equations for the circular cone model [Xie *et*
322 *al.*, 2004].

323 [35] It is interesting to note that $D_{se} = R_c \cos \beta$, showing
324 that halo parameter D_{se} depends on R_c and it increases as
325 time increases. This time-dependent characteristic of D_{se} is
326 determined by the cone apex located at Sun's spherical
327 center (see Figure 2 and the left panels in Figures 3 and 4).
328 There is a circular cone model that lays the apex of the cone
329 model at the solar surface, instead of the spherical center of
330 the Sun assumed here. For this kind of circular cone model,
331 the parameter D_{se} , i.e., the distance between the solar disk
332 center and the elliptic halo center, is a constant [Michalek *et*
333 *al.*, 2003]. This different time variation of D_{se} may be used
334 to determine which circular cone model should be selected

to invert the circular cone model parameters for a specific 335
Type A halo CME. 336

4.2. Solutions of the Inversion Equation System 337

[36] From equation system (8), we have 338

$$\begin{aligned} R_c &= D_{se} / \cos \beta \\ \tan \omega_y &= \frac{-(a - c \sin \beta) + [(a + c \sin \beta)^2 + (4 \sin \beta b^2)]^{0.5}}{2R_c \sin \beta} \\ \tan \chi &= (R_c \tan \omega_y - c) / b \\ \tan \omega_z &= -(a + b \tan \chi) / R_c \sin \beta \end{aligned} \quad (11)$$

Equation system (11) shows that the four unknown model 340
parameters in the left side can be calculated only when the 341
model parameter β as well as the four halo parameters are 342
given. For Types A and B when $\psi = 0$, equation system (11) 343
becomes 344

$$\begin{aligned} R_c &= D_{se} / \cos \beta \\ \tan \omega_y &= SA_{yh} / R_c \\ \tan \omega_z &= -SA_{xh} / (R_c \sin \beta) \end{aligned} \quad (12)$$

The solution of three model parameters R_c , ω_y , and ω_z are 346
determined by the model parameter β and three halo 347
parameters D_{se} , SA_{xh} and SA_{yh} . Expressions (11) and (12) 348
show that as β increases, R_c increases, and ω_y and ω_z 349
decreases when the halo parameters are given. It should be 350
noted that the half angular width ω_z inverted here 351
corresponds to the angle measured clockwise from X_c to 352
the lower side of the cone (see Figure 2). In what follows we 353
show only the inverted value, neglecting its sign. When ω_y 354
 $= \omega_z$, equation system (12) becomes 355

$$\begin{aligned} \sin \beta &= SA_{xh} / SA_{yh} \\ R_c &= D_{se} / \cos \beta \\ \tan \omega &= SA_{yh} / R_c \end{aligned} \quad (13)$$

In this case, three model parameters (ω , R_c , β) can be 357
uniquely determined by three halo parameters (SA_{xh} , SA_{yh} , 358
 D_{se}). Expression (13) is just the inversion solution of the 359
circular cone model derived by Xie *et al.* [2004]. 360

5. Determination of the Propagation Direction 362 and Inversion Solution for Disk FFH CMEs 363

[37] As shown above, the number of unknown model 364
parameters occurred in the solution expressions of the inver- 365
sion equation system is always one more than the number of 366
given halo parameters. The only way to obtain the unique 367
inversion solution of the elliptic cone model is to specify the 368
model parameter β as well as halo parameters. We have 369
pointed out in section 3 that the given halo parameter α , that 370
does not occur in the inversion equation system, contains the 371
information of the model parameters ϕ and λ , and may be 372
used to determine parameter β that depends on ϕ and λ . 373

374 [38] The following two approaches can be used to deter- 435
 375 mine the central axis direction (or the propagation direction) 436
 376 of disk FFH CMEs. Once the parameter β is calculated, the 437
 377 inversion solution of R_c , ω_y , ω_z and χ can be calculated 438
 378 using (11) for Type C and (12) for Types A and B. 439

379 5.1. Two-Point Observation

380 [39] The parameter β can be determined by using two 440
 381 halo CME images observed at the same time by two 441
 382 spacecraft flying on the ecliptic plane. The three modeled 442
 383 halos in the right columns of Figures 3 and 4 are expected to 443
 384 be observed by STEREO A, SOHO, and STEREO B. Any 444
 385 two modeled CME halos provide two values of parameter 445
 386 α , say, α_a and α_b , that contain information of two sets of λ 446
 387 and ϕ for the CME propagation direction. The 447
 388 corresponding two spacecraft are located at the ecliptic 448
 389 plane with their azimuthal difference of $\Delta\phi$. The central 449
 390 axis direction of a CME viewed from any two spacecraft are 450
 391 (λ, ϕ_a) and $(\lambda, \phi_a + \Delta\phi)$. Using equation system (4) we can 451
 392 easily calculate λ , ϕ_a and thus β . For instance, the two 452
 393 modeled halos in top right and middle right panels of 453
 394 Figure 3 show that $\alpha_a = -141.92^\circ$, $\alpha_b = -71.981^\circ$, and 454
 395 $\Delta\phi = 25^\circ$, we obtain $\phi_2 = -20.0^\circ$, $\lambda_2 = 15.00^\circ$ and $\beta_2 =$ 455
 396 65.18° , as shown in the top right panel of Figure 3. They are 456
 397 exactly the same as the original values. 457

398 [40] Using such calculated projection angle β and the 458
 399 values of four given halo parameters D_{se} , SA_{xh} , SA_{yh} and ψ 459
 400 (see the top right panel of Figure 3), the model parameters 460
 401 R_c , ω_y , ω_z and χ can be calculated using equation systems 461
 402 (9) and (11). The parameters β_2 , λ_2 , ϕ_2 , r_{c2} , ω_{y2} , ω_{z2} , and χ_2 462
 403 shown in the top right panel of Figure 3 denote the inverted 463
 404 results. The results shown in middle right and bottom right 464
 405 panels are obtained using the same method for the middle 465
 406 and bottom cases. All three model validation experiments 466
 407 show that expressions (4) and (11) can be used to accurately 467
 408 invert the solution of elliptic cone model parameters for disk 468
 409 FFH CMEs with $\chi \simeq 0$. The red dashed ellipse is calculated 469
 410 using the inverted six model parameters. They completely 470
 411 agree with black ellipse. 471

412 [41] All three black ellipses in Figure 3 are Type A, and 472
 413 produced by the same elliptic cone but with different ϕ . In 473
 414 practice, it is difficult, if not impossible, to determine if a 474
 415 Type A disk FFH CME is formed by a circular or a elliptic 475
 416 cone. To see the difference of inverted circular cone model 476
 417 parameters from the original ones, we first calculate the 477
 418 circular cone model parameters using (13) and three halo 478
 419 parameters (D_{se} , SA_{xh} , SA_{yh}), and then produce the green 479
 420 dotted ellipses on the basis of the inverted model parame- 480
 421 ters. Although the green ellipses are also completely agree 481
 422 with the black ellipses, the obtained values for three circular 482
 423 cone model parameters are totally different from the original 483
 424 elliptic cone model parameters (see left column of Figure 3). 484
 425 For instance, the inverted circular cone model parameters 485
 426 for the top right panel are $R_c = 2.69$, $\omega_y = \omega_z = 57.36$, $\beta =$ 486
 427 38.65 , and $\lambda = 28.79^\circ$, and $\phi = -44.55^\circ$. They are certainly 487
 428 not usable. This experiment shows that even for Type A 488
 429 disk FFH CMEs, it is not safe to use the circular cone model 489
 430 to invert the model parameter. 490

431 [42] Figure 4 is the same as Figure 3, but the values of ω_y , 491
 432 ω_z and χ are different from Figure 3 (see the left column). 492
 433 The red dashed ellipses in the right column of Figure 4 are 493
 434 obtained using the same way as Figure 3 but their agree-

ment with black ellipses is worse than Figure 3. Comparison 435
 of the inverted model parameters with the original ones 436
 show that the parameters λ , ϕ , R_c and ω_y agree with original 437
 ones very well; and dependent on β , the inverted ω_z is 438
 slightly different from original and the inverted χ may be 439
 significantly different from original. 440

5.2. One-Point Observation

441 [43] A CME can propagate in any direction (ϕ , λ) in the 442
 3-D space. For a specified value of α , all possible sets of ϕ 443
 and λ are reduced from whole ϕ - λ plane to a specific curve, 444
 as shown in each panel of Figure 5. The six curves in Figure 445
 5 correspond to the six values of α shown in Figure 1. 446
 These curves are obtained by assuming that the possible 447
 value of β for disk FFH CMEs ranges from 45° to 90° . 448

449 [44] To search for the optimum central axis direction (β or 449
 ϕ_{ce} , λ_{ce}) among all possible directions on a curve 450
 corresponding to a specific value of the halo parameter α , 451
 it is necessary to use additional information that is associ- 452
 ated with the CME propagation direction or the center of 453
 CME source region. 454

455 [45] CME-associated flares or active regions are believed 455
 to be located near the center of CME source region [e.g., 456
Zhao and Webb, 2003], though they are often located near 457
 one leg of CMEs [e.g., *Plunkett et al.*, 2001]. The dot in 458
 each panel of Figure 5 denotes the location of the CME- 459
 associated flare. 460

461 [46] Taking consideration the effect of interaction be- 461
 tween higher-latitude high speed streams and lower-latitude 462
 CME in the declining and minimum phases of solar activity, 463
 it was suggested that the optimum propagation direction 464
 may be found by moving the flare location southwardly, i.e., 465
 by lowering the flare latitude while keeping the flare 466
 longitude constant [*Cremades*, 2005]. This approach cannot 467
 work for all cases shown in Figure 5, especially for the 468
 cases of top left and bottom left panels. In addition, this 469
 approach may not be working for all phases of solar activity. 470

471 [47] We find out the optimum central axis direction 471
 among all possible direction on a curve by finding out the 472
 minimum distance between the dot and the curve in each 473
 panel of Figure 5. The calculated β and $(\phi_{ce}, \lambda_{ce})$ are shown 474
 in the southwest quadrant of each panel. 475

476 [48] It should be noted that the location of flares is often 476
 specified using the latitude and longitude measured in the 477
 heliographic coordinate system, i.e., the latitude and longi- 478
 tude measured with respect to the solar equator, instead of 479
 the solar ecliptic plane. The effect of B0 angle (the helio- 480
 graphic latitude of the Earth) should be corrected before 481
 finding out the optimum model parameter β . The symbols 482
 ϕ_{fs} , λ_{fs} and ϕ_{fe} , λ_{fe} denote longitude and latitude of CME- 483
 associated flares measured in the heliographic and the 484
 heliocentric ecliptic coordinate systems, respectively. We 485
 first calculate ϕ_{fe} , λ_{fe} using ϕ_{fs} , λ_{fs} , and B0, then find out 486
 ϕ_{ce} , λ_{ce} using ϕ_{fe} , λ_{fe} (the dot) and α (the curve). 487

488 [49] Once the optimum value of the projection angle β is 488
 obtained, the model parameters that are supposed to form 489
 the observed halos (white ellipses in Figures 6, 7, and 8) can 490
 be inverted using observed four halo parameters SA_{xh} , SA_{yh} , 491
 D_{se} , and ψ , as shown on the top of each panel in Figure 1. 492
 Figures 6, 7, and 8 display the calculated elliptic cone 493
 model parameters for the six disk FFH CMEs in Figure 1. 494
 The green ellipse in each panel of Figures 6, 7, and 8 is 495

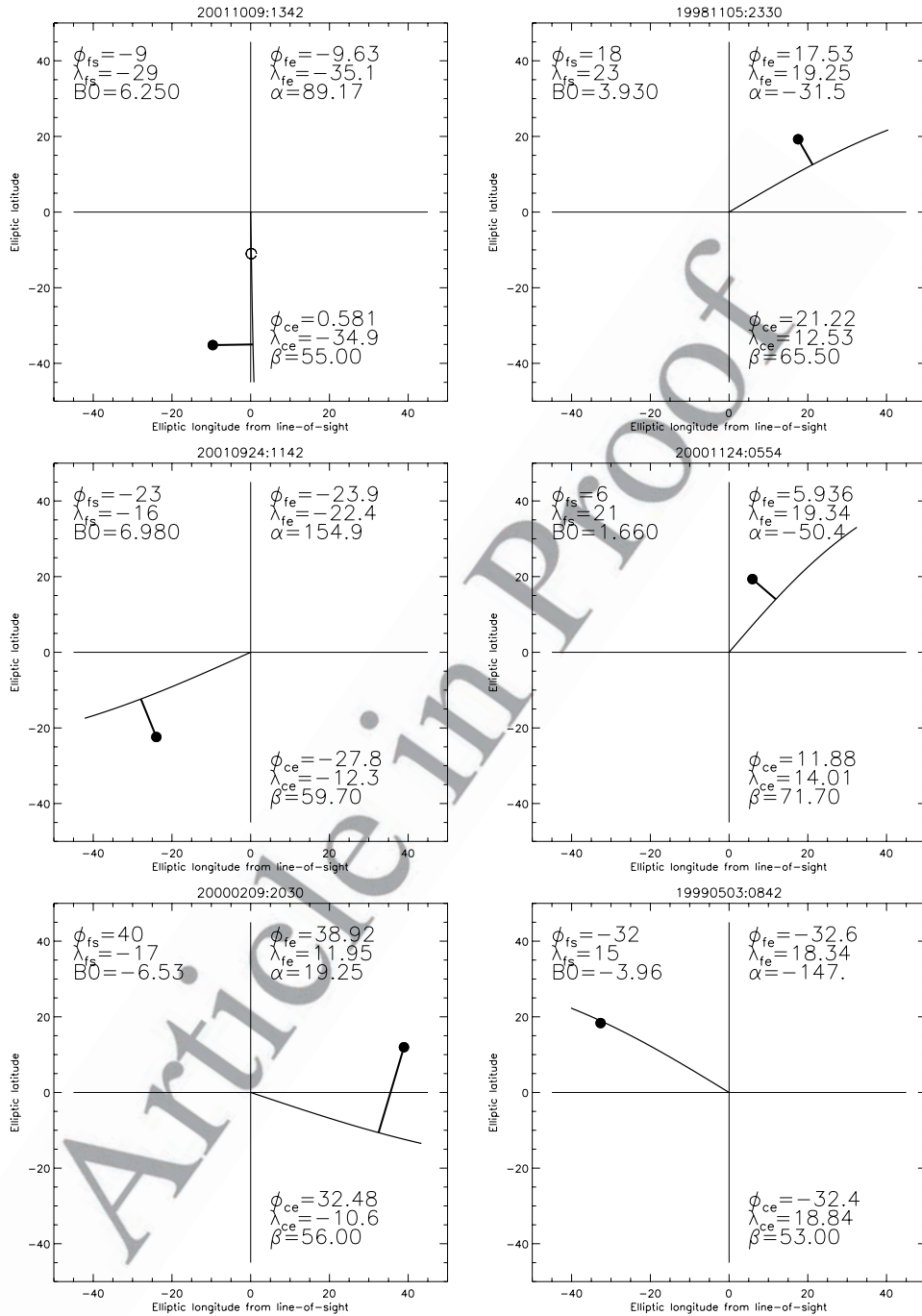


Figure 5. Description of the one-point approach for finding out the CME propagation direction (ϕ_{ce} , λ_{ce}) or β on the basis of halo parameter α and the location of CME-associated flare (ϕ_{fs} , λ_{fs}). See text for details.

496 calculated from the inverted six model parameters and
 497 equation system (5), (6) and (3). The comparison of the
 498 green ellipses with the white ellipses show that the agree-
 499 ment between green and white ellipses depend on the
 500 parameters β and χ . When $\chi < 30^\circ$ the agreement is
 501 reasonable, as shown in Figures 6 and 7. When inverted
 502 $\chi > 30^\circ$ the difference increases as β decreases as shown in
 503 Figure 8. It is similar to what we find out from Figure 4. The
 504 similarity might suggest that the projection angle β obtained
 505 using one-point approach is acceptable.

[50] FFH CMEs of Types B and C can be fitted only by
 506 the elliptic cone model. Type A event, such as the 9 October
 507 2001 event in the top panel of Figure 6, can be formed by
 508 projecting a circular or elliptic base onto the sky-plane, and
 509 thus can be fitted by the elliptic or circular cone model. As
 510 shown by Equations (12) and (13) when $\omega_y = \omega_z$, the
 511 inversion solutions obtained using circular and elliptic cone
 512 models should be the same if the real base is a circular one.
 513 [51] To compare the inversion solutions of the elliptic
 514 cone model with that of the circular cone models, we fit the
 515 Type A halo of the 9 October 2001 using the circular cone
 516

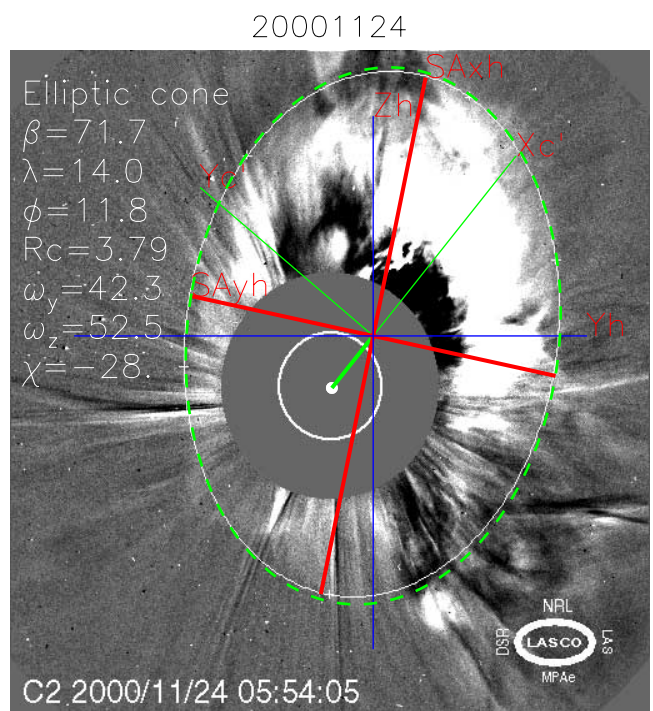
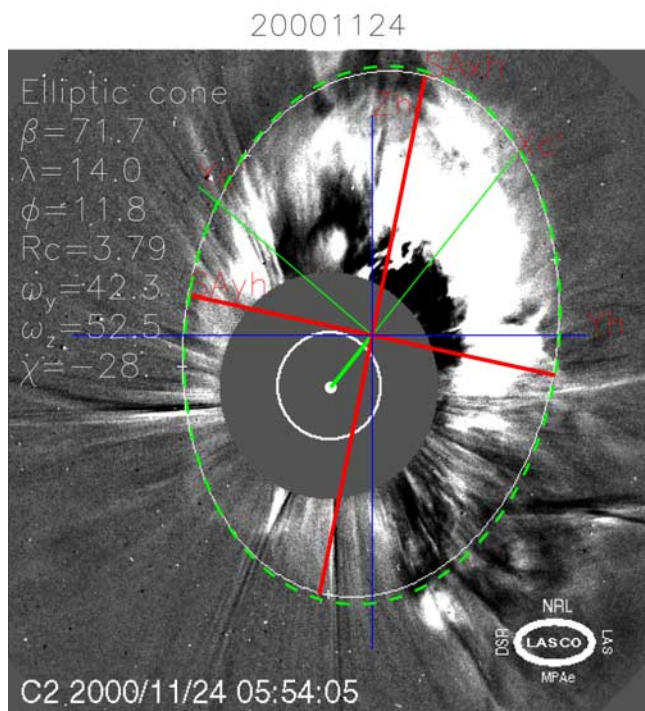
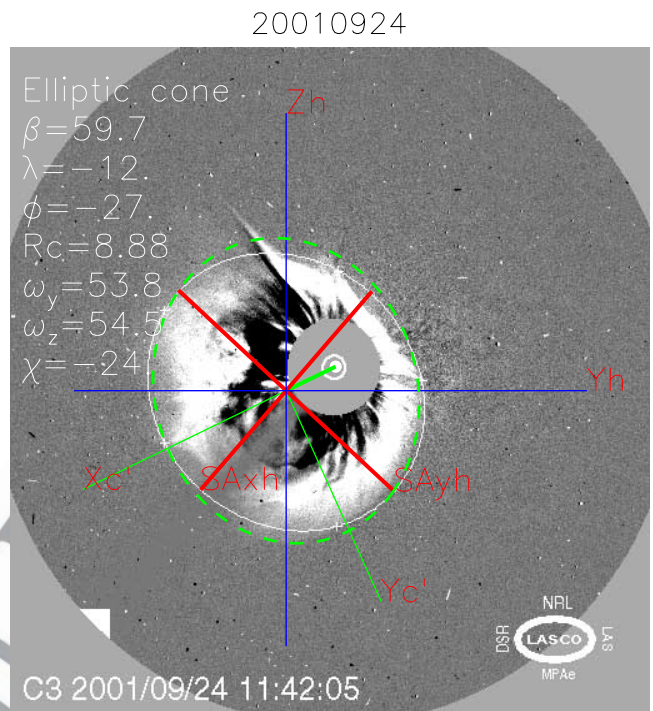
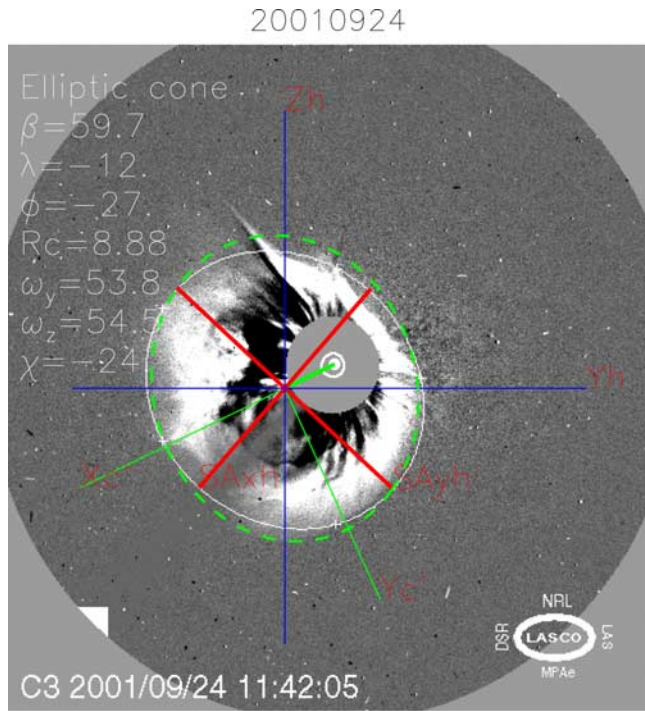


Figure 6. Elliptic and circular cone model parameters inverted using the halo parameters for the two halo events listed in the two top panels of Figure 1 and the parameter β inferred in the two top panels of Figure 4. The green and black dashed ellipses are calculated using the inverted elliptic and circular cone model parameters, respectively.

Figure 7. Elliptic cone model parameters inverted using the halo parameters for the two halo events listed in the two middle panels of Figure 1 and the parameter β inferred in the two middle panels of Figure 4. The green dashed ellipses are calculated using the inverted elliptic cone model parameters.

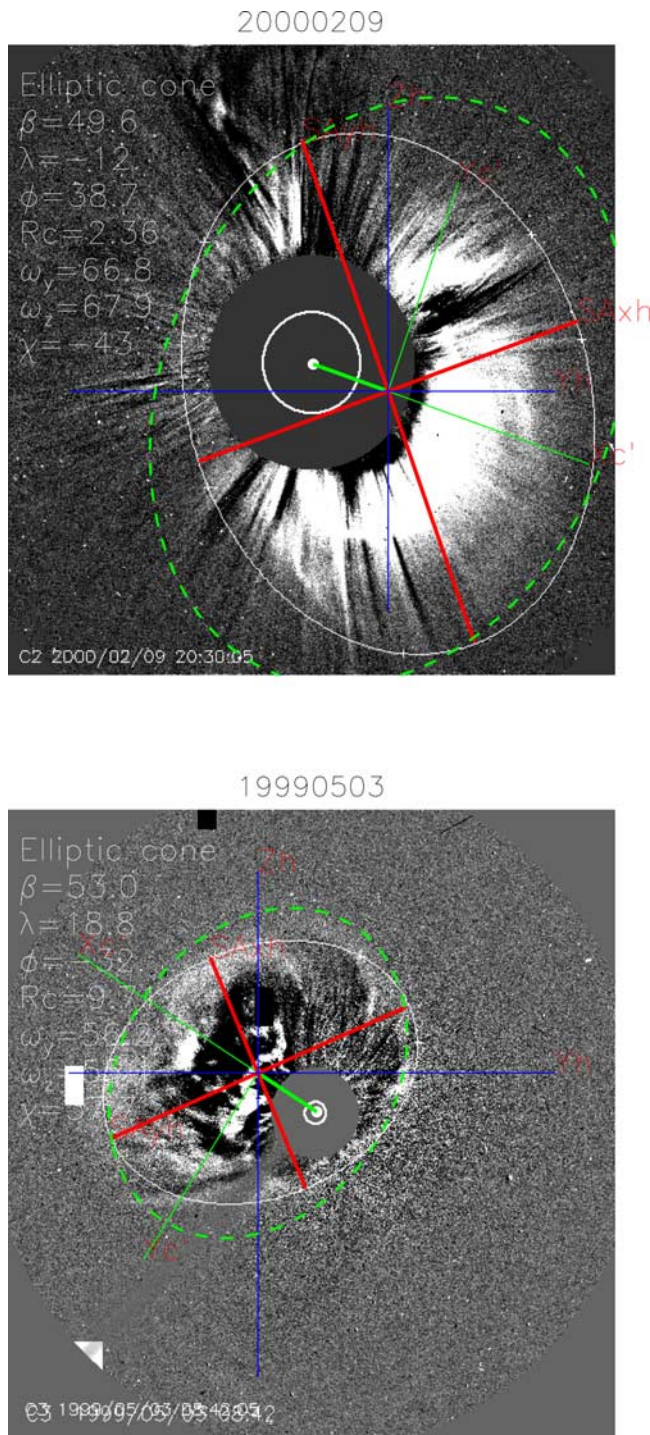


Figure 8. The same as Figure 7, but corresponding to the two halo events listed in the two bottom panels of Figure 1.

517 model as well as the elliptic cone model. Listed in the panel
 518 are the inverted circular cone model parameters as well as
 519 the inverted elliptic cone model parameters. The black
 520 dashed ellipse is obtained using the circular cone model
 521 parameters. Although the agreement of both the green and
 522 black ellipses with the observed white ellipse is equally
 523 well, the elliptic cone model parameters are significantly
 524 different from the circular cone model parameters. The
 525 central axial direction inverted from the circular cone model

(the open circle in the top left panel of Figure 5) is located 526
 far from the CME-associated flare location (the black dot), 527
 and the distance from the solar center to the elliptic base, 528
 $R_c = 18.4$ solar radii, appears to be too far from the solar 529
 surface to produce observed brightness of the halo CME. 530
 Therefore the Type A halo of the 9 October 2001 event is 531
 caused by the elliptic cone model, instead of the circular 532
 cone model. 533
 534

6. Summary and Discussions

[52] We have shown that on the sky-plane $Y_h Z_h$, disk 536
 FFH CMEs provide five halo parameters, and can be 537
 classified into Types A, B, and C, depending on the major 538
 axis of elliptic halos being perpendicular to, aligned with, or 539
 anywhere else from the direction from the solar disk center 540
 to the CME halo center. 541

[53] The elliptic cone model needs six model parameters 542
 to characterize its morphology in the heliocentric ecliptic 543
 coordinate system $X_h Y_h Z_h$. 544

[54] However, the morphology of the CME halo and the 545
 elliptic cone base in the projection coordinate system $X'_c Y'_c$ 546
 Z'_c can be described by four halo and five model parameters, 547
 respectively. In the system $X'_c Y'_c Z'_c$, the halo parameter α 548
 disappears, and the two model parameters λ and ϕ that 549
 denote the CME propagation direction in $X_h Y_h Z_h$ are 550
 replaced by one new model parameter β , the projection 551
 angle. 552

[55] On the other hand, the axis Y'_c is the reference axis for 553
 measuring the orientation of both elliptic CME halos and 554
 elliptic cone bases. The inversion equation system of the 555
 elliptic cone model and its solution can thus be established 556
 by setting $\delta_h = \delta_b + \Delta\delta$, and assuming $\Delta\delta = \delta_h - \delta_b \simeq \psi -$ 557
 χ , and by comparing the like term in the expressions 558
 between modeled and observed halos in the $X'_c Y'_c Z'_c$ 559
 system. 560

[56] The halo parameter α that does not occur in the 561
 inversion equation system depends on both latitude and 562
 longitude of the CME propagation direction (λ, ϕ), and has 563
 been used to estimate the model parameter β on the basis of 564
 two-point or one-point observations of halo CMEs. 565

[57] The two-point approach uses two values of α observed 566
 at the same time by COR1 and COR2 on board 567
 STEREO A and B. Model validation experiments have been 568
 carried out for the cases of $\chi = 0^\circ$ and $\chi = -30^\circ$. The 569
 experiment results show that the CME propagation direction 570
 can be accurately determined by the two-point approach. 571
 The other four model parameters can also be accurately 572
 inverted for the case of $\chi = 0^\circ$, i.e., for Types A and B disk 573
 FFH CMEs. For the case of $\chi = -30^\circ$, i.e., Type C disk 574
 FFH CMEs, the obvious difference occurs only between 575
 inverted and original parameter χ , the orientation of the 576
 elliptic cone base. These results imply that the difference is 577
 caused by the assumption of $\Delta\delta = \delta_h - \delta_b \simeq \psi - \chi$, that is 578
 made in establishing the inversion equation system (8). 579

[58] The one-point approach combines the value of α 580
 with such simultaneous observation as the location of CME- 581
 associated flare, which includes the information associated 582
 with CME propagation direction. The six events displayed 583
 in Figure 1 for showing the three types of disk FFH CMEs 584
 have been tested. Both the propagation direction obtained 585
 using one-point approach and the other four model param- 586

587 eters inverted appear to be reasonable and acceptable. The
 588 agreement between the observed halos and modeled halos
 589 depends mainly on the projection angle β . It is the same as
 590 what we find in the model validation experiments for the
 591 two-point approach. The STEREO data are expected to be
 592 used to finally determine in what extent the CME propaga-
 593 tion direction obtained from the one-point approach is
 594 correct.

595 [59] After obtaining the elliptic cone model parameters,
 596 the CME propagation speed can be determined using the
 597 method similar to *Zhao et al.* [2002] or *Xie et al.* [2004].

598 [60] The inversion equation system of the elliptic cone
 599 model and the expression of its solution can be reduced to
 600 that of the circular cone model. For Type A modeled halos
 601 in Figure 3 and observed halos in Figure 6, three circular
 602 cone model parameters are also inverted on the bases of
 603 three halo parameters. Both results show significant differ-
 604 ences from the inverted elliptic cone model parameters,
 605 though the modeled halos calculated using the circular cone
 606 model parameters completely agree with the observed halos.

607 [61] It is difficult, if not impossible, to distinguish halos
 608 produced by elliptic cone from that by circular cone. The
 609 circular cone model should be used with utmost care lest it
 610 leads to erroneous conclusions. The inverted elliptic cone
 611 model parameters should be the same as the inverted
 612 circular cone model parameters if the base of the cone-like
 613 CME structure is circular. It is suggested to use the elliptic
 614 cone model to invert the geometric and kinematic properties
 615 for all Type A disk FFH CMEs.

616 [62] There are some disk FFH CMEs that are not purely
 617 elliptic. Some of them may be formed by ice-cream cone
 618 models. It has been shown that by determining the halo
 619 parameters from the rear part of the asymmetric halos, the
 620 elliptic cone model presented here can still be used to invert
 621 the model parameters for these asymmetric disk FFH CMEs
 622 (X. P. Zhao, Ice cream cone models for halo coronal mass
 623 ejections, manuscript in preparation, 2008).

624 [63] The accuracy of inversion solutions depends signif-
 625 icantly on the halo parameters measured from observed disk
 626 FFH CMEs. We have developed codes to calculate the five
 627 halo parameters on the basis of the outer edge of halo
 628 CMEs. All the white elliptic outer edge shown in Figure 1
 629 were determined using the five-point technique (see
 630 *Cremades* [2005] for details). To further improve the accu-
 631 racy of the halo parameters we plan to automatically and
 632 more objectively recognize the outer edge of disk FFH CMEs
 633 using the pattern or feature recognition technique.

[64] **Acknowledgments.** We thank H. Cremades for sending us her
 Ph.D. thesis and her data product for 30 disk FFH CMEs. The six images in
 Figure 1 are selected from the 30 disk FFH CMEs. This work is supported
 by NASA grants NAGW 2502 and NAG5-3077 and by NSF grant
 ATM9400298.

[65] Amitava Bhattacharjee thanks David Webb and Gang Li for their
 assistance in evaluating this paper.

References

- Cremades, H. (2005), Three-Dimensional Configuration and Evolution of
 Coronal Mass Ejections, Ph.D. thesis, Copernicus, Katlenburg-Lindau,
 Germany. 642
 Cremades, H., and V. Bothmer (2005), Geometrical properties of coronal
 mass ejections, in *Coronal and Stellar Mass Ejections: Proceedings of*
IAU Symposium 226, edited by K. P. Dere, J. Wang, and Y. Yan, pp. 48–
 54, Int. Astron. Union, Paris. 643
 Gopalswamy, N., A. Lara, S. Yashiro, S. Nunes, and R. A. Howard (2003),
 Coronal mass ejection activity during solar cycle 23, in *Proceedings of*
the ISCS 2003 Symposium on Solar Variability as an Input to Earth's
Environment, Eur. Space Agency Spec. Publ., ESA-SP 535, 403–414. 644
 Gopalswamy, N., S. Yashiro, and S. Akiyama (2007), Geoeffectiveness of
 halo coronal mass ejections, *J. Geophys. Res.*, *112*, A06112, doi:10.1029/
 2006JA012149. 645
 Howard, R. A., D. J. Michels, N. R. Sheeley Jr., and M. J. Koomen (1982),
 The observation of a coronal transient directed at Earth, *Astrophys. J.*,
263, L101–L104. 646
 Michalek, G., N. Gopalswamy, and S. Yashiro (2003), A new method for
 estimating widths, velocities, and source location of halo coronal mass
 ejections, *Astrophys. J.*, *584*, 472–478. 647
 Odstrcil, D., and V. J. Pizzo (1999), Distortion of the interplanetary mag-
 netic field by three-dimensional propagation of coronal mass ejections in
 a structured solar wind, *J. Geophys. Res.*, *104*(A12), 28,225–28,240. 648
 Odstrcil, D., P. Riley, and X. P. Zhao (2004), Numerical simulation of the
 12 May 1997 interplanetary CME event, *J. Geophys. Res.*, *109*, A02116,
 doi:10.1029/2003JA010135. 649
 Plunkett, S. P., et al. (2001), Solar source regions of coronal mass ejections
 and their geomagnetic effects, *J. Atmos. Sol. Terr. Phys.*, *63*, 389–402. 650
 Riley, P., C. Schatzman, H. V. Cane, I. G. Richardson, and N. Gopalswamy
 (2006), On the rates of coronal mass ejections: Remote solar and in situ
 observations, *Astrophys. J.*, *647*, 648. 651
 Sheeley, N. R., Jr., W. N. Hakala, and Y.-M. Wang (2000), Detection of
 coronal mass ejection associated shock waves in the outer corona,
J. Geophys. Res., *105*(A3), 5081–5092. 652
 Xie, H., L. Ofman, and G. Lawrence (2004), Cone model for halo CMEs:
 Application to space weather forecasting, *J. Geophys. Res.*, *109*, A03109,
 doi:10.1029/2003JA010226. 653
 Zhao, X. P. (2005), Determination of geometrical and kinematical proper-
 ties of frontside halo coronal mass ejections, in *Coronal and Stellar Mass*
Ejections: Proceedings of IAU Symposium 226, edited by K. P. Dere,
 J. Wang, and Y. Yan, pp. 42–47, Int. Astron. Union, Paris. 654
 Zhao, X. P., and D. F. Webb (2003), Source regions and storm effectiveness
 of frontside full halo coronal mass ejections, *J. Geophys. Res.*, *108*(A6),
 1234, doi:10.1029/2002JA009606. 655
 Zhao, X. P., S. P. Plunkett, and W. Liu (2002), Determination of geometrical
 and kinematical properties of halo coronal mass ejections using the cone
 model, *J. Geophys. Res.*, *107*(A8), 1223, doi:10.1029/2001JA009143. 656

X. P. Zhao, W. W. Hansen Experimental Physics Laboratory, Stanford
 University, Stanford, CA 94305-4085, USA. (xuepu@sun.stanford.edu) 690
 691